This article has been accepted for publication in a future issue of this journal, but has not been fully edited. Content may change prior to final publication. IEEE Transactions on Robotics, 2020.

Design of Multi-Degree-of-Freedom Microrobots Driven by Homogeneous Quasi-Static Magnetic Fields

Sajad Salmanipour, *Student Member, IEEE,* Omid Youssefi, *Student Member, IEEE,* and Eric Diller, *Member, IEEE*

***Abstract*—Wireless robots at the sub-centimeter size are often actuated using externally-generated magnetic fields. For most applications, these remote magnetic microrobots are located relatively far from the magnetic field generation sources. In this condition, all microrobots receive approximately the same driving magnetic field (which we term a *homogeneous* field). While some solutions have been presented to allow for the creation of simple on-board tools, the full potential of the *homogeneous* magnetic field for multi degrees of freedom (DOF) actuation has not been exploited.**

Here we introduce a design framework to utilize the maximum number of independently controlled DOFs on a microrobot system. We make use of three classes of mechanisms which are commonly used in practice and allow for more complex microrobots with up to eight DOFs. To verify the functionality of our framework, we used it to design an optimized drug delivery robot equipped with a 3-DOF drug-releasing mechanism and a 4-DOF motion mechanism. Experiments were performed to actuate each one of the robot's seven DOFs individually, where the cross-talk error between these seven DOFs averaged 7% with a max error of 18.3%.

***Index Terms*—Microrobot, multi-robot systems, medical robots and systems, magnetic actuation.**

I. Introduction

Recent developments of wireless microrobots (here defined as robotic devices smaller than one centimeter in overall size) show their potential in applications such as drug delivery [1], minimally invasive surgery [2] and micro-assembly systems [3] among others [4]. A variety of methods such as chemical [5], optical [6], thermal [7] and magnetic-based techniques [8] have successfully been utilized to enable actuation and control at microscale [4]. Magnetic actuation has the advantage of transmitting relatively large forces and torques wirelessly at the microscale, while allowing for the design of sophisticated microrobotic motions and activation of on-board mechanisms [9]. The ability to transmit magnetic fields safely into the human body makes magnetic actuation an appealing actuation method for biomedical applications.

An additional advantage of magnetic actuation is the capability for multi Degrees Of Freedom (DOF) addressable actuation. Controllable DOFs in a microrobot system can include motion of one or more microrobots in three dimensional (3D) space as well as the motion of on-board mechanisms such as grippers. Through clever system design, each DOF can be independently actuated to allow for pose control (position and orientation) of a single microrobot [10], [11], independent control of the position of multiple microrobots [12], [13] and the actuation of dexterous microrobots with on-board bending deformation and tools [14], [15], [2]. Various methods have been suggested in the literature to enable the independent actuation of multiple system DOFs in magnetic microrobots. One approach is to use time-varying magnetic fields [16] (as opposed to quasi-static magnetic fields which can be assumed to be constant over short time periods), where clever mechanical "decoding" systems convert magnetic forces and torques into multiple desired motions. One example is the design of systems with different resonant frequencies, where each microrobot reacts to a specific excitation frequency [17]. Although requiring a mechanical "decoding" mechanism, time-varying field solutions require microrobot mechanism which exhibit highly non-linear responses, are often complex, and can be sensitive to small errors. These systems have thus not been capable of controlling more than three DOFs. Another method allowing for multi-DOF microrobotic control is to utilize interaction forces between magnetic agents [18]. This approach however, requires precise sensory feedback on microrobot pose which limits its practical applications. The use of magnetic fields which vary over the workspace (which we call *heterogeneous* magnetic fields) is another approach for developing multi-DOF magnetic microdevices [13], [19], [12], [20]. In this method, microrobots are spaced out over the workspace. Each microrobot experiences a different magnetic field, and consequently are able to move/rotate independently. This method relies on large variation in field over the workspace, which requires magnetic field generation sources to be close to the workspace. Many microrobotic applications (such as inside the human body) will necessitate the field generation sources to be placed far from the workspace, limiting the effectiveness of using this *heterogeneous* field method. None of the existing magnetic multi-DOF actuation methods can be easily generalized to arbitrary microrobotic platforms, and thus the field is in need of a general approach which can be used in all magnetic microrobots where fields may be relatively uniform over the workspace.

When field generation sources are located relatively far from the small microrobot workspace, the magnetic field (actuation input) can be assumed to be the same for every point in the workspace. We call this field a *homogeneous* magnetic field. *Homogeneous* magnetic fields will be especially seen in medical applications where the field generation sources are

S. Salmanipour, O. Youssefi and E. Diller are with the Department of Mechanical and Industrial Engineering, University of Toronto, Ontario, Canada. E-mail: ediller@mie.utoronto.ca.

Manuscript received June 24, 2019; revised February 13, 2020.

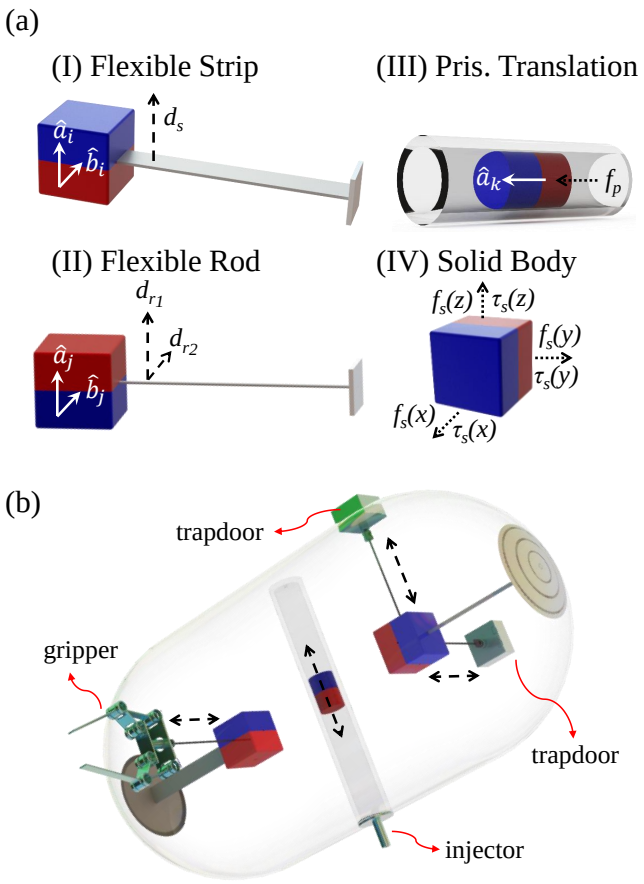

Fig. 1. (a) Four classes of simple magnetic mechanisms; dashed lines represent free axes and solid white arrows are force/torque projection unit vectors. (I) 1-DOF flexible strip; d_s: deflection value (scalar), $\hat{a}_i$: force projection vector, $\hat{b}_i$: torque projection vector. (II) 2-DOF flexible rod; d_{r1}/d_{r2}: deflection values (scalars), $\hat{a}_j$: force/torque projection vector, $\hat{b}_j$: torque/force projection vector. (III) 1-DOF prismatic translation (shown here as a magnet moving in a cylinder); f_p: prismatic force (scalar), $\hat{a}_k$: force projection vector. (IV) 6-DOF unconstrained solid body; $\vec{f}_s$: force vector, $\vec{\tau}_s$: torque vector. (b) An exemplified general microrobot equipped with four on-board tools.

located outside of the patient's body and a small region inside the body is the targeted workspace. In this work, we make a *homogeneous* magnetic field assumption, which makes this study more inclusive. In other words, the method introduced here can be utilized for both *homogeneous* and *heterogeneous* magnetic fields.

Homogeneous magnetic fields have successfully been used in developing multi-DOF microrobot systems. In multi-DOF magnetic microrobots, a variety of different mechanisms are utilized to convert magnetic forces and torques on embedded magnets into desired motions. Here we study four classes of common magnetic mechanisms, which are overviewed in Fig. 1(a): (I) Magnets mounted on the end of a free strip with one unconstrained deflection axis (1-DOF). In this mechanism, the output (to be controlled) is the scalar d_s which represents the deflection value. An example of this mechanism is a microgripper where two 1-DOF flexible strips act as the arms of the gripper which opens and closes in response to the magnetic field [21]. (II) Magnets mounted on the end of a free beam with two free deflection axes (2-DOF). Here we have two scalar outputs d_{r1}/d_{r2} representing deflection values. This class of mechanism is commonly found in minimally-invasive surgical tool applications where magnets attached to flexible rods provide 2-DOF of bending motion, specifically useful in developing magnetic steerable catheters [22], [2], [23]. (III) Prismatic translation of a magnet on a spring or in a tube (1-DOF); the term "prismatic" refers to the unconstrained linear motion of a joint which allows translation without rotation. In this case, to avoid difficult-to-model friction and fluid drag, we consider the scalar output to be prismatic force f_p. An example of this is in the biopsy capsules developed by Yim et al. [15] and Son et al. [14], where 1-DOF prismatic flexible magnetic linkages are used to perform biopsy tasks. (IV) Unconstrained solid body (6-DOF), where scalar outputs are three forces $(f_s(x), f_s(y), f_s(z))$ producing translational motion and three torques $(\tau_s(x), \tau_s(y), \tau_s(z))$ producing rotation. The body of mobile microrobots experience this motion class. An unconstrained rigid magnetic body has six free axes, and depending on the geometry of its magnetization profile, at least five [8], [10], [24] and a maximum of six [11], [25] of its free axes can be controlled using magnetic field.

Although all of the previously mentioned magnetic mechanisms have successfully been incorporated into microdevices to achieve a high level of dexterity, existing magnetic microrobots typically have only up to two on-board controlled DOFs and up to six solid body motion DOFs. No demonstrated magnetic microrobot has exhibited more than six total actuated DOFs, and many applications would benefit from even more sophisticated mechanism motions requiring more actuated DOFs. In addition, there has been no definition of the maximum number of magnetic actuation DOFs, nor a fundamental framework for the design of microrobots which utilize the maximum number of actuated DOFs.

In our previous conference paper [26], we investigated *homogeneous* quasi-static magnetic fields and their capabilities for actuation of magnetic mechanisms. We showed that the maximum possible number of actuated DOFs in *homogeneous* quasi-static magnetic fields is eight. That work demonstrated a simple proof-of-concept magnetic mechanism with eight controlled DOFs. However, that work did not show how to design a microrobot which utilizes these "unlocked" magnetic field capabilities, and the demonstration mechanism was not a functional robot. As a complement to that conference paper, here we introduce a design framework for developing magnetic microrobots with the maximum number of DOFs to achieve maximum dexterity. As a case study, we utilize this framework to develop a 7-DOF magnetic drug delivery robot prototype. The proposed design framework is based on the four introduced types of common magnetic mechanisms. Starting with designer-defined information including the number of magnets and types and quantity of mechanisms, the design algorithm presented results in an optimized design solution giving the positions and orientations of magnets as well as the layout of the on-board mechanisms.

This design framework can be used in applications where the targeted workspace is not accessible, and wireless microdevices (actuated by an external *homogeneous* quasi-static

magnetic field) are required to perform high dexterity tasks; for example in drug delivery robots, biopsy microdevices, wireless surgical tools, and others. As an example case study, in this work we utilize the presented framework to design a dexterous drug delivery robot prototype.

Modern pharmaceuticals featuring low bio-availability and poor water solubility are increasingly emerging, where their short therapeutic life time and poor stability would benefit from more advanced delivery methods [27]. As a result, the progressing area of developing new drug delivery systems is receiving significant attention recently [28], [29], [1]. This has led to a wide variety of potential applications such as targeted drug delivery to ocular system [30], olfactory region [31], neural probes [32] and insulin administration [33]. Delivery of drugs within the gastrointestinal (GI) tract with advanced functionality is of particular interest [34], [35], [36].

A drug delivery capsule device would benefit from a motion mechanism to place the capsule at a desired location, and a releasing mechanism to perform controlled drug release. Some studies have focused on motion mechanisms and some others have put their efforts in developing releasing mechanisms [1]; but, only a few have succeeded in designing microdevices with active control of both motion and releasing mechanisms [34], [37]. The main challenge is the limited space available inside the capsules which must contain the power source, positioning and releasing mechanism. Magnetically-driven activation is thus appealing, where remotely delivered power (by an external magnetic field) exerts forces and torques on the magnets inside the capsule, acting as an input control signal for both motion and releasing systems [37], [36]. Here we utilize our multi-DOF magnetic actuation framework to design a wireless drug delivery robot prototype. This robot features a 4-DOF positioning mechanism to move the robot toward its desired location, and a 3-DOF drug release mechanism.

In the following sections, we first introduce the concept of how we mathematically model magnetic mechanisms. Then we briefly review the *homogeneous* magnetic field parameters and how they generate forces and torques on remote magnetic bodies. Next, our general framework is formed as a design optimization problem, which solves for the optimal configuration of discrete magnets with minimum required actuation input and minimum interaction forces and torques. The functionality of our multi-DOF magnetic actuation framework is demonstrated next through the development of a millimeter-scale mobile robot prototype with seven actuated DOFs. The paper ends with experimental results demonstrating the independent actuation of each of the seven DOFs of the robot.

II. Concept and Magnetic Actuation Fundamentals

The useful microrobotic mechanism classes we are studying in this work are shown in Fig. 1(a). Each mechanism requires a single on-board magnet, and so a multi-DOF microrobotic system can consist of one or up to eight individual magnets depending on which mechanisms are used. We consider single-robot systems in this paper, consisting of a single body with a number of on-board mechanisms. As the robot body rotates, all of the on-board mechanisms rotate with it. This constraint on the orientations of on-board mechanisms allows us to maintain independent magnetic control of these mechanisms if they are properly designed.

Fig. 1(b), illustrates an example of using multiple on-board mechanisms in one microrobot, where a 1-DOF flexible strip is actuating a gripper, a 2-DOF flexible rod opens two trapdoors and a 1-DOF prismatic mechanism is used for drug injection. In this exemplified device, a total of four DOFs are used by these on-board mechanisms. As the maximum number of controllable DOFs for any microdevice actuated under *homogeneous* quasi-static magnetic fields is eight [26], there remains four additional controllable DOFs, which could be used for controlling position and/or orientation of the body of the robot. Thus, the total number of controllable DOFs on a microrobot consist of the on-board mechanism DOFs plus the controlled DOFs for the body of the robot.

The primary method of this paper (preliminarily introduced in our conference paper [26]) is to utilize all available components of the *homogeneous* magnetic field at a point to control multiple independent DOFs. As a magnetic field has eight independent usable components (three field components and five field gradient components) at every point in space, a properly designed robot could exploit all components for independent control of up to eight DOFs. It has been shown that all eight magnetic fields can be controlled using a properly designed field generation system [38]. As the magnetic effect on an individual magnet will depend on the orientation of that magnet as well as the class of mechanism to which it is attached, we can design each mechanism in a microrobotic system to use a different combination of magnetic field components and thus have each mechanism be individually controllable.

Now we introduce the mathematical description of this magnetic actuation (a glossary of variables is provided at the end of the paper). First we briefly review the relationship between magnetic field parameters and the effect on each individual magnet. The magnetic field will exert a force and torque on each magnet. The magnet will experience a torque which attempts to rotate the magnet into alignment with the field direction, and a force which pulls the magnet according to the shape of the magnetic field. A matrix mapping the eight magnetic field parameters (inputs to our robotic system) to the six force/torque elements for each magnet (outputs) is defined here [8], which will be utilized in our design framework for developing multi-DOF magnetic microdevices.

In a magnetic field $\vec{B} = \begin{bmatrix} B_x & B_y & B_z \end{bmatrix}^\top$, a rigid magnetic body with magnetic moment $\vec{m} = \begin{bmatrix} m_x & m_y & m_z \end{bmatrix}^\top$, experiences a torque $\vec{\tau}$ and a force $\vec{f}$. By utilizing the skew-symmetric matrix $\mathbf{S}(\vec{m})$ to represent the cross product [38] (required for torque calculations), the torque $\vec{\tau}$ on a single magnet is calculated as:

$$\vec{\tau} = \mathbf{S}(\vec{m})\ \vec{B} \tag{1}$$

$$\text{where}\quad \mathbf{S}(\vec{m}) = \begin{bmatrix} 0 & -m_z & m_y \\ m_z & 0 & -m_x \\ -m_y & m_x & 0 \end{bmatrix}.$$

The force vector $\vec{f}$ is generated by the field spatial gradient. The magnetic field spatial gradient matrix has nine elements which by utilizing Maxwell equations, it can be written in terms of five independent elements [38]; $\nabla \cdot \vec{B} = 0$ requires the gradient matrix to have a zero trace and $\nabla \times \vec{B} = 0$ forces it to be symmetric. By assembling these five independent spatial gradient terms into a vector $\vec{g} = \begin{bmatrix} \frac{\partial B_x}{\partial x} & \frac{\partial B_x}{\partial y} & \frac{\partial B_x}{\partial z} & \frac{\partial B_y}{\partial y} & \frac{\partial B_y}{\partial z} \end{bmatrix}^\top$, as formulated by Petruska and Nelson (2015) [38], the force on a single magnet is calculated as:

$$\vec{f} = \mathbf{F}(\vec{m})\ \vec{g} \tag{2}$$
$$\text{where} \quad \mathbf{F}(\vec{m}) = \begin{bmatrix} m_x & m_y & m_z & 0 & 0 \\ 0 & m_x & 0 & m_y & m_z \\ -m_z & 0 & m_x & -m_z & m_y \end{bmatrix}.$$

By utilizing equations (1) and (2), the force and torque vectors can be presented together as a wrench, where the full input is assembled into a vector $\vec{U} = \begin{bmatrix} \vec{g} & \vec{B} \end{bmatrix}^\top$. The force and torque are then assembled together as:

$$\begin{bmatrix} \vec{f} & \vec{\tau} \end{bmatrix}^\top = \mathbf{K}(\vec{m})\ \vec{U} \tag{3}$$
$$\text{where} \quad \mathbf{K}(\vec{m}) = \begin{bmatrix} \mathbf{F}(\vec{m}) & \mathbf{0}_{3\times 3} \\ \mathbf{0}_{3\times 5} & \mathbf{S}(\vec{m}) \end{bmatrix}.$$

Here $\mathbf{K}(\vec{m})$ is a 6×8 matrix which maps field inputs to force and torque outputs, and $\mathbf{0}_{3\times 3}$ and $\mathbf{0}_{3\times 5}$ are zero matrices.

To generate the input vector $\vec{U}$, electromagnetic coils [8], [26], permanent magnets [10], or combinations of both can be used. It has been shown that at least eight magnets are required to generate these eight components [38]. More details of the generation of these field components for the eight-electromagnetic system used in this paper are given in the *Magnetic Field Generation* subsection (IV. B.).

III. Multi-DOF Magnetic Actuation Framework

Discrete on-board magnets attached to the body of the microrobot, experience forces and torques which are used for both controlling the individual on-board mechanisms' DOFs and microrobot solid body DOFs. We assume the microrobot is comprised of n_{strip} 1-DOF flexible strips, n_{rod} 2-DOF flexible rods and n_{slider} 1-DOF prismatic sliders. The overall system output $\vec{Y}$, includes flexible strip deflections $d_{s_{i=1,2,..,n_{\text{strip}}}}$, rod deflections $d_{r1_j}/d_{r2_{j=1,2,..,n_{\text{rod}}}}$, prismatic forces $f_{p_{k=1,2,..,n_{\text{slider}}}}$, solid body selected forces $\vec{f}_{\text{sel}}$ and solid body selected torques $\vec{\tau}_{\text{sel}}$, as:

$$\vec{Y}_{n_D\times 1} = \begin{bmatrix} d_{s_i}\ ,\cdots,\ d_{r1_j},\ d_{r2_j}\ ,\cdots,\ f_{p_k}\ ,\cdots,\ \vec{f}_{\text{sel}}^{\top},\ \vec{\tau}_{\text{sel}}^{\top} \end{bmatrix}^\top \tag{4}$$

$$n_D = n_{\text{strip}} + 2n_{\text{rod}} + n_{\text{slider}} + n_{\text{sp}} + n_{\text{so}}$$

where n_{sp} and n_{so} are the lengths of the $\vec{f}_{\text{sel}}$ and $\vec{\tau}_{\text{sel}}$ vectors, respectively (maximum of 3 for each), and n_D represents the microrobot total number of DOFs, including individual on-board mechanisms' DOFs (strips/rods/sliders) and solid body position/orientation DOFs. Note that among six available solid body forces and torques, only selected ones $(\vec{f}_{\text{sel}}, \vec{\tau}_{\text{sel}})$ are placed inside the output vector (to be controlled). The magnetic actuation input is the $\vec{U}$ field vector from eq. (3), and the system matrix $\mathbf{H}$ maps this input vector to outputs as:

$$\vec{Y} = \mathbf{H}_{n_D\times 8}\ \vec{U}. \tag{5}$$

It can be noted from this equation that the maximum number of DOFs that can be independently controlled is equal to the maximum possible rank for the $\mathbf{H}$ matrix, which is eight [26]. This eight DOFs are actuated by the five independent gradient components (generating translational forces), and three magnetic field components (generating rotational torques). Flexible strips and rods can be actuated by using both translational forces and rotational torques, whereas prismatic sliders and solid body selected forces are only actuated through translational forces. Therefore, one must carefully consider the fact that the number of DOFs which are actuated only through translational motion cannot exceed five.

The system matrix $\mathbf{H}$ is determined by the type and arrangement of mechanisms chosen. We break these down into two categories: 1) *designer variables* specified by the designer and 2) *geometric optimization variables*, to be solved for in the design of an optimized microrobot. The designer variables include the quantity of discrete magnets, the types of on-board mechanisms, and selected position/orientation DOFs to be controlled for the microdevice solid body. In determining these predefined designer variables, users must consider the fact that the magnetic force decays faster than magnetic torque as coil distances to targeted workspace increases[26]. In other words, based on the specific field generation limitations one might consider the general rule that on-board mechanisms which are actuated only through translational forces should not require the largest forces. The geometric variables to be optimized are the configuration of each magnet and the orientation of each mechanism. The geometric optimization variables are determined through an optimization process which must maintain a full rank $\mathbf{H}$ matrix (allowing for independent actuation of all desired DOFs), while minimizing the electromagnet coil currents required to actuate all of the mechanisms, as well minimizing undesirable interaction forces/torques between on-board magnets.

In this section we show how the system matrix $\mathbf{H}$ can be calculated. We build the system matrix from each individual controllable DOF by finding the matrix mapping the input vector $\vec{U}$ to each individual term of the output vector $\vec{Y}$. These individual matrices will be concatenated to form the complete system matrix. Next, the optimization problem is introduced which solves for an optimum configuration of on-board magnets by varying the geometric optimization variables.

A. System Matrix

Here we first investigate how each class of physical constraints (Fig. 1(a)), converts magnetic inputs into desired mechanism motions (deflections for flexible strip/rod mechanisms and sliding forces for prismatic mechanisms). Next, we calculate the robot body outputs (selected forces/torques) as a function of the magnetic inputs, and combine all of these relationships into the overall system matrix.

1) 1-DOF Flexible Strip: A permanent magnet attached to a flexible strip can freely move along a single axis $\hat{a}_i$ as shown in Fig. 1(a)(I). Assuming small deflections (as compared to the length of the strip), the magnet orientation remains fixed during translation. The deflection of the i^{th} strip (d_{s_i}) is created by magnetic forces $\vec{f}(\vec{m}_i)$ projected in the $\hat{a}_i$ direction and torques $\vec{\tau}(\vec{m}_i)$ projected about the $\hat{b}_i$ axis as:

$$d_{s_i} = \alpha_i \hat{a}_i^\top \vec{f}(\vec{m}_i) + \beta_i \hat{b}_i^\top \vec{\tau}(\vec{m}_i) \tag{6}$$

which by using equation (3) can be written as:

$$\begin{aligned} &d_{s_i} = \begin{bmatrix} \alpha_i \hat{a}_i^\top & \beta_i \hat{b}_i^\top \end{bmatrix} \mathbf{K}(\vec{m}_i)\ \vec{U} \\ &\text{for} \quad i = 1, 2, \cdots, n_{\text{strip}}. \end{aligned} \tag{7}$$

Here, α_i and β_i are constant scalars converting forces and torques to deflections, which can be calculated as:

$$\alpha_i = \frac{l_i^3}{3E_i I_i} \quad \text{and} \quad \beta_i = \frac{l_i^2}{2E_i I_i} \tag{8}$$

where l_i represents length of the i^{th} beam, E_i is its elastic modulus and I_i is the corresponding moment of inertia.

2) 2-DOF Flexible Rod: A magnet attached to a flexible rod is free to move along two axes of motion $\hat{a}_i$ and $\hat{b}_i$ as shown in Fig. 1(a)(II). These two deflections of the j^{th} rod (d_{r1_j}/d_{r2_j}) are given as:

$$\begin{bmatrix} d_{r1_j} \\ d_{r2_j} \end{bmatrix} = \alpha_j \begin{bmatrix} \hat{a}_j^\top \\ \hat{b}_j^\top \end{bmatrix} \vec{f}(\vec{m}_j) + \beta_j \begin{bmatrix} \hat{b}_j^\top \\ -\hat{a}_j^\top \end{bmatrix} \vec{\tau}(\vec{m}_j) \tag{9}$$

using equation (3) we have:

$$\begin{aligned} &\begin{bmatrix} d_{r1_j} \\ d_{r2_j} \end{bmatrix} = \begin{bmatrix} \alpha_j \hat{a}_j^\top & \beta_j \hat{b}_j^\top \\ \alpha_j \hat{b}_j^\top & -\beta_j \hat{a}_j^\top \end{bmatrix} \mathbf{K}(\vec{m}_j)\ \vec{U} \\ &\text{for} \quad j = 1, 2, \cdots, n_{\text{rod}}. \end{aligned} \tag{10}$$

3) 1-DOF Prismatic Translation Mechanism: The last mechanism is a magnet sliding inside a tube as shown in Fig. 1(a)(III). The prismatic force (f_{p_k}) for the k^{th} slider moving along axis $\hat{a}_k$, can be calculated as:

$$f_{p_k} = \hat{a}_k^\top \vec{f}(\vec{m}_k) \tag{11}$$

and by using equation (3):

$$\begin{aligned} &f_{p_k} = \begin{bmatrix} \hat{a}_k^\top & \mathbf{0}_{1\times 3} \end{bmatrix} \mathbf{K}(\vec{m}_k)\ \vec{U} \\ &\text{for} \quad k = 1, 2, \cdots, n_{\text{slider}}. \end{aligned} \tag{12}$$

4) Solid Body Pose Control: By applying an external magnetic field, the microdevice rigid body receives a total force $\vec{f}_s$ and a total torque vector $\vec{\tau}_s$, calculated as:

$$\begin{aligned} &\begin{bmatrix} \vec{f}_s \\ \vec{\tau}_s \end{bmatrix} = \mathbf{A}(\vec{m}_i, \vec{m}_j, \vec{m}_k)\ \vec{U}, \quad \text{where} \\ &\mathbf{A}(\vec{m}_i, \vec{m}_j, \vec{m}_k) = \\ &\sum_{i=1}^{n_{\text{strip}}} \mathbf{C}_i \mathbf{K}(\vec{m}_i) + \sum_{j=1}^{n_{\text{rod}}} \mathbf{C}_j \mathbf{K}(\vec{m}_j) + \sum_{k=1}^{n_{\text{slider}}} \mathbf{C}_k \mathbf{K}(\vec{m}_k). \end{aligned} \tag{13}$$

Here the $\mathbf{C}$ matrices are 6×6 transmission matrices, to calculate transmitted forces and torques to the microdevice solid body from all on-board magnets. For the 1-DOF flexible strip mechanism, the transmission matrix $\mathbf{C}_i$ can be calculated as:

$$\mathbf{C}_i = \begin{bmatrix} \mathbf{I}_{3\times 3} & \mathbf{0}_{3\times 3} \\ \mathbf{S}(\vec{p}_i) & \mathbf{I}_{3\times 3} \end{bmatrix} \tag{14}$$

where $\mathbf{I}$ is the identity matrix and $\vec{p}_i$ represents the position of the i^{th} magnet w.r.t. microrobot center of mass. For the 2-DOF flexible rod mechanism, transmission matrix is defined as:

$$\mathbf{C}_j = \begin{bmatrix} \mathbf{I}_{3\times 3} & \mathbf{0}_{3\times 3} \\ \mathbf{S}(\vec{p}_j) & \mathbf{I}_{3\times 3} \end{bmatrix}. \tag{15}$$

The transmission matrix for the 1-DOF prismatic translation mechanism is defined as:

$$\mathbf{C}_k = \begin{bmatrix} \mathbf{I} - \hat{a}_k \hat{a}_k^\top & \mathbf{0}_{3\times 3} \\ \mathbf{S}(\vec{p}_k)(\mathbf{I} - \hat{a}_k \hat{a}_k^\top) & \mathbf{I} - \hat{a}_k \hat{a}_k^\top \end{bmatrix}. \tag{16}$$

For a general application requiring n_{sp}-DOF position and n_{so}-DOF orientation control for the solid body of the microdevice, we must select n_{sp} elements from the $\vec{f}_s$ vector, and n_{so} elements from the $\vec{\tau}_s$ vector. By choosing $\vec{f}_{\text{sel}}$ and $\vec{\tau}_{\text{sel}}$ as vectors containing the selected terms, we have:

$$\begin{bmatrix} \vec{f}_{\text{sel}} \\ \vec{\tau}_{\text{sel}} \end{bmatrix} = \begin{bmatrix} \mathbf{E1}_{n_{\text{sp}}\times 3} & \mathbf{0}_{n_{\text{sp}}\times 3} \\ \mathbf{0}_{n_{\text{so}}\times 3} & \mathbf{E2}_{n_{\text{so}}\times 3} \end{bmatrix} \begin{bmatrix} \vec{f}_s \\ \vec{\tau}_s \end{bmatrix} \tag{17}$$

which by inserting equation (13) can be written as:

$$\begin{bmatrix} \vec{f}_{\text{sel}} \\ \vec{\tau}_{\text{sel}} \end{bmatrix} = \begin{bmatrix} \mathbf{E1} & \mathbf{0} \\ \mathbf{0} & \mathbf{E2} \end{bmatrix} \mathbf{A}(\vec{m}_i, \vec{m}_j, \vec{m}_k)\ \vec{U} \tag{18}$$

where $\mathbf{E1}/\mathbf{E2}$ are predefined selecting matrices, with three columns (corresponding to three scalar forces/torques) and $n_{\text{sp}}/n_{\text{so}}$ rows; in each of their rows appears one "1" (selected force/torque) and two "0" (unselected forces/torques).

5) Overall System Matrix: By inserting equations (7), (10), (12) and (18) into equations (4) and (5), the system matrix is formed as:

$$\mathbf{H}_{n_D\times 8} = \begin{bmatrix} \begin{bmatrix} \alpha_{i=1}\hat{a}_{i=1}^\top & \beta_{i=1}\hat{b}_{i=1}^\top \end{bmatrix} \mathbf{K}(\vec{m}_{i=1}) \\ \vdots \\ \begin{bmatrix} \alpha_{i=n_{\text{strip}}}\hat{a}_{i=n_{\text{strip}}}^\top & \beta_{i=n_{\text{strip}}}\hat{b}_{i=n_{\text{strip}}}^\top \end{bmatrix} \mathbf{K}(\vec{m}_{i=n_{\text{strip}}}) \\ \begin{bmatrix} \alpha_{j=1}\hat{a}_{j=1}^\top & \beta_{j=1}\hat{b}_{j=1}^\top \\ \alpha_{j=1}\hat{b}_{j=1}^\top & -\beta_{j=1}\hat{a}_{j=1}^\top \end{bmatrix} \mathbf{K}(\vec{m}_{j=1}) \\ \vdots \\ \begin{bmatrix} \alpha_{j=n_{\text{rod}}}\hat{a}_{j=n_{\text{rod}}}^\top & \beta_{j=n_{\text{rod}}}\hat{b}_{j=n_{\text{rod}}}^\top \\ \alpha_{j=n_{\text{rod}}}\hat{b}_{j=n_{\text{rod}}}^\top & -\beta_{j=n_{\text{rod}}}\hat{a}_{j=n_{\text{rod}}}^\top \end{bmatrix} \mathbf{K}(\vec{m}_{j=n_{\text{rod}}}) \\ \begin{bmatrix} \hat{a}_{k=1}^\top & \mathbf{0}_{1\times 3} \end{bmatrix} \mathbf{K}(\vec{m}_{k=1}) \\ \vdots \\ \begin{bmatrix} \hat{a}_{k=n_{\text{slider}}}^\top & \mathbf{0}_{1\times 3} \end{bmatrix} \mathbf{K}(\vec{m}_{k=n_{\text{slider}}}) \\ \begin{bmatrix} \mathbf{E1} & \mathbf{0} \\ \mathbf{0} & \mathbf{E2} \end{bmatrix} \mathbf{A}(\vec{m}_i, \vec{m}_j, \vec{m}_k) \end{bmatrix} \tag{19}$$

B. Optimization Problem

Our systematic approach for designing multi-DOF microrobots includes an optimization of the design to achieve a full rank system matrix (which will impose design constraints), with maximum singular values (minimum required actuation inputs) while minimizing the interaction forces and torques between the on-board magnets. These singular values and interaction forces and torques, will thus be used to form an optimization cost function.

For an application with less than eight controlled DOFs, the system matrix is not square, and the number of controllable outputs is equal to the rank of the $\mathbf{H}$ matrix. By applying singular value decomposition method (reduced form) we have:

$$\begin{aligned} &\mathbf{H} = \mathbf{W}_{n_D \times r}\ \mathbf{S}_{r\times r}\mathbf{V}^{\top}_{r\times 8} \\ &\mathbf{S} = \text{diag}(\sigma_1, \sigma_2, \cdots, \sigma_r) \\ &\text{rank}(\mathbf{H}) = r \end{aligned} \tag{20}$$

where the σ_i's are the singular values and their number r represents the system matrix rank. To solve for an optimized configuration of mechanisms resulting in a full rank $\mathbf{H}$ matrix with the maximum possible singular values and minimum interaction forces and torques between magnets, the following cost function is defined:

$$cost = \prod_{i=1}^{r} |\sigma_i^{-1}| \ + \ \gamma\ (f_{\text{int}} + \lambda \tau_{\text{int}}) \tag{21}$$

where γ and λ are weight adjusting scalars. The first term in the cost function is to punish small singular values, and the last two terms are scalar functions representing interaction forces (f_{int}) and interaction torques (τ_{int}), defined as:

$$\begin{aligned} f_{\text{int}} &= \sum_{i=1}^{n_{\text{mag}}} \sum_{j=1}^{n_{\text{mag}}} \left\| (\vec{m}_i \cdot \nabla)\vec{B}(\vec{m}_j) \right\| \quad i \neq j \\ \tau_{\text{int}} &= \sum_{i=1}^{n_{\text{mag}}} \sum_{j=1}^{n_{\text{mag}}} \left\| \vec{m}_i \times \vec{B}(\vec{m}_j) \right\| \quad i \neq j \end{aligned} \tag{22}$$

Here n_{mag} is the total number of magnets placed inside the microdevice. In order to investigate the scaling properties, we must consider the relationship between the forces/torques and magnets' sizes and their distance w.r.t. each other. Considering two similar cubic magnets (width w), located at a distance of h from each other, the following relationships can be derived: $\frac{f_{\text{int}}}{f_{\text{act}}} \propto \frac{w^3}{h^4}$, $\frac{\tau_{\text{int}}}{\tau_{\text{act}}} \propto \frac{w^3}{h^3}$; where f_{act} and τ_{act} are magnitude of actuation forces and torques (generated by the external magnetic field) and f_{int} and τ_{int} are undesired interaction forces and torques. For example if magnets' sizes are doubled and we still want to have the same $f_{\text{int}}/f_{\text{act}}$ ratio, their distance (robot size) should be increased by a factor of $2^{0.75}$ (nonlinear), and if our concern is to have the same $\tau_{\text{int}}/\tau_{\text{act}}$ ratio, their distance should be doubled (linear). As a result for any specific application, as soon as the magnets' sizes are determined (through application requirements), the robot overall size and the feasibility of the design can be verified.

We introduce Table I, to summarize all of the variables in this process. Predefined designer variables are type and quantity of controlled DOFs ($n_{\text{strip}}, n_{\text{rod}}, n_{\text{slider}}, n_{\text{sp}}, n_{\text{so}}$), robot size ($\rho$), weight adjusting scalars (λ, γ), and magnets' strengths ($\|\vec{m}_i\|, \|\vec{m}_j\|, \|\vec{m}_k\|$). The geometric optimization variables are the embedded magnets' orientations ($\hat{m}_i, \hat{m}_j, \hat{m}_k$), their positions ($\vec{p}_i, \vec{p}_j, \vec{p}_k$) and physical constraints on the mechanisms denoted by the unit vectors ($\hat{a}_i, \hat{a}_j, \hat{a}_k, \hat{b}_i, \hat{b}_j$). Considering size of three for each vector, dimension of the search is equal to: $12\ n_{\text{strip}} + 12\ n_{\text{rod}} + 9\ n_{\text{slider}}$. With the cost function defined in equation (21) and the constraints introduced in the Table I, the overall optimization problem is defined as:

TABLE I
DESIGN VARIABLES FOR MICROROBOT OPTIMIZATION; USER SETS PREDEFINED DESIGN VARIABLES, WHILE THE OPTIMIZATION CODE SOLVES FOR THE GEOMETRIC OPTIMIZATION VARIABLES CONSIDERING THE PREDEFINED CONSTRAINTS.

Designer Variables	Geom. Optim. Variables	Constraints
n_{strip}, n_{rod}, n_{slider}	$\hat{m}_i$, $\hat{m}_j$, $\hat{m}_k$	$\left\|\hat{m}_{i,j,k}\right\| = \left\|\hat{a}_{i,j,k}\right\| = \left\|\hat{b}_{i,j}\right\| = 1$
n_{sp}, n_{so}	$\vec{p}_i$, $\vec{p}_j$, $\vec{p}_k$	$\left\|\vec{p}_{i,j,k}\right\| \leq \rho$
ρ, λ, γ	$\hat{a}_i$, $\hat{a}_j$, $\hat{a}_k$	$\hat{a}_i^{\top}\hat{b}_i = \hat{a}_j^{\top}\hat{b}_j = 0$
$\|\vec{m}_i\|$, $\|\vec{m}_j\|$, $\|\vec{m}_k\|$	$\hat{b}_i$, $\hat{b}_j$	$\vec{m}_{i,j,k} = \left\|\vec{m}_{i,j,k}\right\| \hat{m}_{i,j,k}$
		$\text{rank}(\mathbf{H}) = n_D = r$

$$\min_{\hat{m},\vec{p},\hat{a},\hat{b}} \quad \prod_{i=1}^{r} |\sigma_i^{-1}| \ + \ \gamma\ (f_{\text{int}} + \lambda \tau_{\text{int}}) \tag{23}$$

$$\text{subject to} \begin{cases} \|\hat{m}_{i,j,k}\| = \|\hat{a}_{i,j,k}\| = \left\|\hat{b}_{i,j}\right\| = 1 \\ \|\vec{p}_{i,j,k}\| \leq \rho \\ \hat{a}_i^{\top}\hat{b}_i = \hat{a}_j^{\top}\hat{b}_j = 0 \\ \vec{m}_{i,j,k} = \|\vec{m}_{i,j,k}\|\, \hat{m}_{i,j,k} \\ \text{rank}(\mathbf{H}) = n_D = r \end{cases}$$

Here the constraints in the first set define directional unit vectors. The second set is an inequality constraint which limits the distance of the magnets from the center of the microrobot. The third set are to ensure that force and torque projection vectors (specific to flexible strips and rods) are perpendicular as specified in Fig. 1. The fourth set are to specify magnetic moment magnitudes as defined by the designer, and the final constraint is to enforce a full rank system matrix.

IV. Case Study: Drug Delivery Robot Capsule Prototype

In our previous work [26], we showed that the maximum possible independently controllable DOFs actuated remotely in a *homogeneous* quasi-static magnetic field is eight, and a simple proof of concept demonstration mechanism, comprised of cubic magnets attached to Nitinol wires, was developed to verify our claim experimentally. However, that proof of concept mechanism was not a functional robot, and a design framework for developing functional magnetic microrobots with maximum DOFs was lacking.

In this work we introduced the missing design framework, and to demonstrate the functionality of the presented design

framework, here in this section and as an example case study, we present the design of a dexterous drug delivery robot prototype. This millimeter-scale prototype has a 4-DOF motion mechanism, with control over its x-y position and yaw-$pitch$ orientation, as well as three drug release mechanisms capable of releasing three different drug chambers independently.

The presented drug delivery robot in this work utilizes only class III and IV mechanisms, where the releasing system is made using class III (Prismatic Translation) and the pose control is formulated by using the class IV (Solid Body). The effectiveness of the first two classes (Flexible Strip and Flexible Rod mechanisms) were verified in our previous work [26], where an 8-DOF mechanism was built by utilizing flexible links, and a maximum cross-talk of 8.6% was reported.

A. Capsule Prototype Design

Among the three classes of constrained magnetic mechanisms illustrated in Fig. 1(a), the cylindrical magnet with translational motion is well-suited for drug release purposes; the force along tube axis can be used for injection, and the constraint side wall forces can be used to control the robot's solid body motions. Thus, we choose three releasing mechanisms which are comprised of three magnets ($n_{\text{slider}} = 3$), each moving freely inside a cylinder. To avoid prototyping complexities related to custom magnetization profiles, we decided to add one more constraint set (in addition to constraint sets in eq. (23)) by choosing axially magnetized cylindrical magnets, making the tubes' axes aligned with the magnetization directions, i.e.:

$$\hat{m}_k = \hat{a}_k \quad \text{for} \quad k = 1, 2, 3 \tag{24}$$

There are no type I or type II mechanisms, so $n_{\text{strip}} = 0$ and $n_{\text{rod}} = 0$. The capsule positioning mechanism includes 2-DOF position control ($n_{\text{sp}} = 2$), and a 2-DOF orientation control ($n_{\text{so}} = 2$) for the solid body of the microrobot. The selected axes for position control are x and y, and for orientation control are $pitch$ (rotation around x axis) and yaw (rotation around z axis). Therefore, selection matrices for position control (**E1**) and orientation control (**E2**) are defined as:

$$\mathbf{E1} = \begin{bmatrix} 1 & 0 & 0 \\ 0 & 1 & 0 \end{bmatrix} \quad \text{and} \quad \mathbf{E2} = \begin{bmatrix} 1 & 0 & 0 \\ 0 & 0 & 1 \end{bmatrix}. \tag{25}$$

The optimum design must result in a full rank $\mathbf{H}$ matrix, mapping the eight field inputs to the seven desired outputs, including three injection forces $(f^*_{p_1}, f^*_{p_2}, f^*_{p_3})$, two solid body translational forces $(f^*_{\text{sel}}(x), f^*_{\text{sel}}(y))$ and two solid body rotational torques $(\tau^*_{\text{sel}}(x), \tau^*_{\text{sel}}(z))$. The optimization search includes a total of 18 free variables: 9 variables for magnets' orientations $\hat{a}_k$ (3 directional unit vectors) and 9 variables for their positions $\vec{p}_k$ (3 vectors). To find the optimized solution resulting in minimum interaction forces and torques and maximum singular values for $\mathbf{H}$ matrix, the MATLAB *fmincon* function (Global Optimization Toolbox, sqp algorithm, 25 sec process time) was utilized. The optimized configuration is shown in Fig. 2. This configuration includes two cylinders on x-y plane (± 60 degrees away from y axis), and one on the y-z plane (120 degrees away from y axis). The full optimization details including predefined designer variables and the optimized configuration solution are reported in Table II.

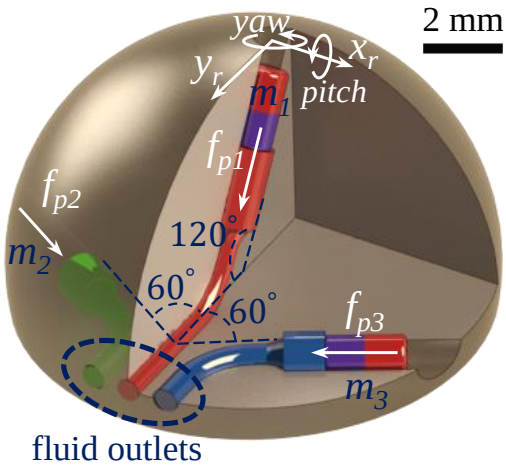

Fig. 2. Schematic of the optimized drug delivery robot. Three cylindrical magnets are denoted as m_{1-3}. The seven vectors (in white) represent the independently-controllable DOFs of the robot. Design is symmetric w.r.t. the y axis, and details of the configuration solution can be found in Table II.

TABLE II
DRUG DELIVERY ROBOT OPTIMIZATION PROBLEM; PREDEFINED DESIGNER VARIABLES AND THE GENERATED OPTIMIZED GEOMETRIC DESIGN SOLUTION. VECTORS ARE REPRESENTED IN THE ROBOT COORDINATE FRAME $[x_r\ y_r\ z_r]$, ATTACHED TO THE CENTER OF THE ROBOT.

Designer Variables	Optimized Geometric Solution
$n_{\text{strip}} = n_{\text{rod}} = 0$, $n_{\text{slider}} = 3$	$\vec{p}_1^{\top} = [0.0\ \ 0.0\ \ +4.5]$ mm
$n_{\text{sp}} = n_{\text{so}} = 2$	$\vec{p}_2^{\top} = [-3.9\ \ -2.25\ \ 0.0]$ mm
$\rho = 4.5$ mm	$\vec{p}_3^{\top} = [+3.9\ \ -2.25\ \ 0.0]$ mm
$\lambda = 885$	$\hat{a}_1^{\top} = [0.0\ \ -0.5\ \ +0.866]$
$\gamma = 2.8 \times 10^{23}$	$\hat{a}_2^{\top} = [-0.866\ \ -0.5\ \ 0.0]$
$\|\vec{m}_{1-3}\| = 8.8 \times 10^{-4}$ Am^2	$\hat{a}_3^{\top} = [+0.866\ \ -0.5\ \ 0.0]$

B. Magnetic Field Generation

After the design is generated and built, we generate a desired control input $\vec{U}_{\text{des}}$ using our previously-developed field generation system with eight electromagnetic coils [26]. Since the $\mathbf{H}$ matrix is not square, its pseudo-inverse $\mathbf{H}^{\dagger}$ is used to calculate control input vector $\vec{U}_{\text{des}}$ for a desired set of outputs $\vec{Y}_{\text{des}}$, therefore we have:

$$\vec{U}_{\text{des}} = \mathbf{H}^{\dagger}\ \vec{Y}_{\text{des}} \tag{26}$$
$$\vec{Y}_{\text{des}} = \left[f^*_{p_1}, f^*_{p_2}, f^*_{p_3}, f^*_{\text{sel}}(x), f^*_{\text{sel}}(y), \tau^*_{\text{sel}}(x), \tau^*_{\text{sel}}(z)\right]^{\top}.$$

As shown in Fig. 3, this system has four inner coils and four outer coils, and considering 3 kW input power limit, it can generate three magnetic field components as large as 15 mT, and five gradient components as large as 0.55 T/m. The coil currents $\vec{I}$ can be calculated as:

$$\vec{I} = \mathbf{L}^{-1}\ \vec{U}_{\text{des}} \tag{27}$$

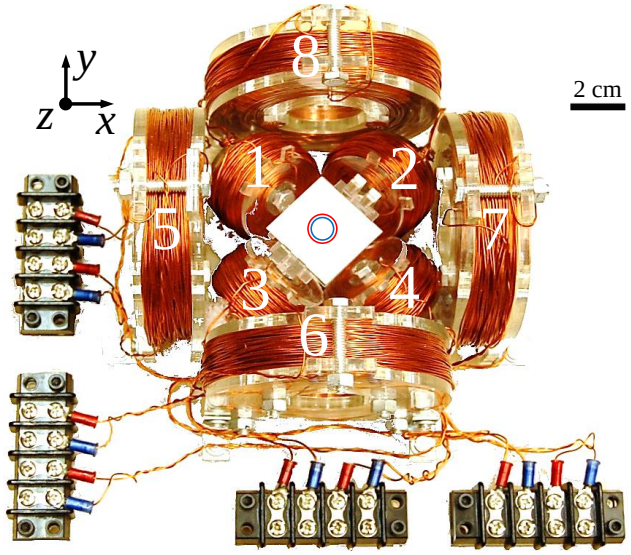

Fig. 3. Electromagnetic coil system; consisted of four inner coils which are tilted upward 30 degrees from the horizontal toward the workspace center, and four outer coils with their axes on the x-y plane. The blue circle in the workspace represents the microrobot and the red circle demonstrates the region where eight magnetic field parameters are less than 30% different w.r.t. their nominal values at the center.

where $\mathbf{L}$ is the coil matrix mapping eight coil currents to eight desired magnetic field parameters. The systematic procedure to calculate this $\mathbf{L}$ matrix can be found in our previous work [26].

As reported in the Table II, on-board magnets are positioned at 4.5 mm away from the robot center. Based on the coil system geometry, it is expected that the on-board magnets will receive a magnetic field with up to 23% error. Therefore, this field production error will be the primary source for the cross-talk error. Since the on-board magnets cannot be placed closer to each other (due to interaction forces and torques), the only solution to reduce this systematic cross-tall error is to use a bigger coil system where the coils are located at a relatively far distance from the workspace, and consequently the magnets will receive a more homogeneous magnetic field. However, due to time and budget limitations this field generation system was deemed adequate to demonstrate the principle.

C. Fabrication

In order to realize the design presented in Fig. 2, which is a transparent half-sphere with 12 mm diameter, UV stereolithography (SLA) 3D printing was utilized (Formlabs Form2) as shown in Fig. 4. This method of fabrication was selected due to its intricate fabrication capability required to create the 3D internal features of this microrobot. These features include cylindrical channels to house 1 mm cylindrical NdFeB magnets and outlet channels which are 600 μm in diameter. The prototype microrobot was fabricated using Form 2 Clear Resin with 25 μm layer height. The resin consists of Methacrylate oligomers and monomer with photoinitiators for curing. The mechanical properties of the cured material closely resemble those of PMMA. Since the features are small, it was observed that print orientation significantly influences the print quality.

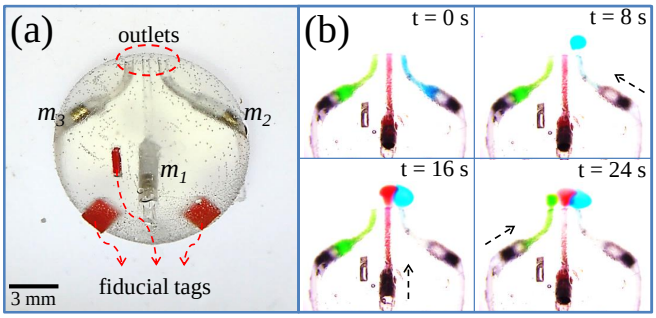

Fig. 4. (a) 7-DOF drug delivery microrobot prototype. (b) Validating 3-DOF drug release mechanism; each cylinder is activated for 8 s with a constant 200 μN desired translational force acting on cylindrical magnets. Video is available in supplementary materials.

At certain orientation, especially when the channels run parallel to the build platform, print failure occurs. As the resolution of the printer (Form 2) was barely sufficient to produce this microrobot, the print orientation was chosen using a systematic trial and error method. The manufacturer-recommended post-cure fabrication steps were followed producing the final body of the microrobot. The three cylindrical magnets were then inserted into their respective channels and end stops were placed to prevent the magnets from escaping the body.

D. Experimental Results

To verify microrobot's functionalities, including both motion and release mechanisms, two experiments were conducted. For each experiment, a 2 cm clear acrylic cubic container was placed in the center of the coil system to provide a fluid environment for the microrobot. The first experiment was to test the three injection mechanisms where water was used as the fluid environment, and the second experiment was designed to verify the independent controllability of all the seven DOFs, where the acrylic container was filled with corn syrup mixed with water. As shown in Fig. 4(a), three fiducial tags were used to visually track the position (x, y) and orientation (yaw, $pitch$) of the capsule using cameras and machine vision. Two stationary cameras (FO134TC, Foculus, 30 fps) provided a top view (x-y plane) and side view (y-z plane) of the workspace. To overcome friction forces, an optional high frequency oscillating field along the y axis (1 mT magnitude), calculated as: $\vec{B}_{\text{ag}} = \begin{bmatrix} 0 & \sin(60\pi t) & 0 \end{bmatrix}^\top$ mT, was used to agitate cylindrical magnets inside tube chambers.

The injection mechanism was examined first where the acrylic cubic container was filled with water, providing the fluid environment for the robot. Although water allows for successful drug injections at relatively small prismatic forces, controlling the position and orientation of the microrobot in such a low viscosity environment requires a high feedback rate (our 30 fps cameras are not adequate to track the capsule motion; we expect 60 fps is required). As a result, and for this injection experiment only, we used tape to fix the robot position and orientation at the workspace center. An unconstrained motion demonstration will be shown in the next section. Three cylindrical magnets (NdFeB N50, 1 mm diameter, 1 mm

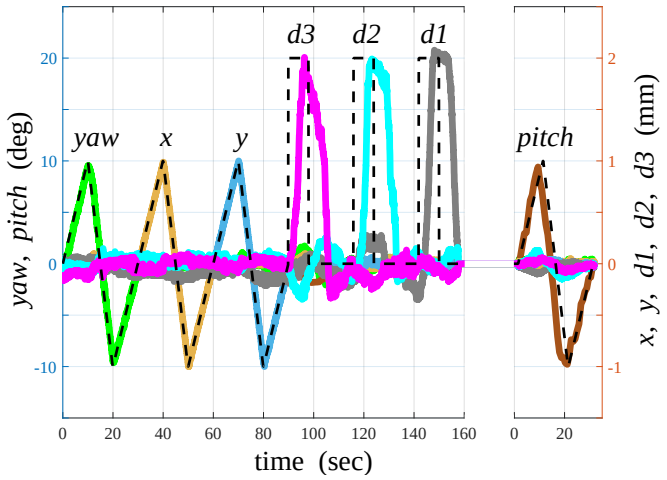

Fig. 5. Validating 7-DOF drug delivery robot. During actuation period, the targeted DOF follows the reference trajectory (dashed line), while other six DOFs remain close to zero. Video is available in supplementary materials.

height) were inserted into the tube chambers. The three drug delivery reservoirs were filled with food coloring dye of three colors to simulate three different drugs loaded into the microrobot. The desired injection forces to inject the simulated drugs out were set using trial and error method because they depend on fluid drag and friction which are difficult to reliably model. These were set as $f^*_{p_1} = f^*_{p_2} = f^*_{p_3} = 200$ μN. Each of the magnets were actuated one after another, and as shown in Fig. 4(b), three colored liquids were injected into the environment, independently. Note that in this experiment $\vec{B}_{ag}$ was disabled.

The second experiment was conducted to show that all of the seven DOFs are independently controllable. The acrylic cubic container was filled with corn syrup mixed with water (ratio of 10:3 respectively), providing a viscus fluid environment for the robot to freely slide under its surface. Fluid viscosity of 110 mPa.S (at 20° C) was measured by observing the falling speed of a metal sphere in the fluid, and comparing the speed with the same sphere falling in a calibrated silicone oil. Three magnetic tubes (NdFeB N50, 1 mm outside diameter, 0.5 mm inside diameter, 1 mm height) were inserted inside its chambers, and each of the seven controllable DOFs were then actuated in sequence one after the other while keeping the other six DOFs stationary, as shown in Fig. 5. As mentioned previously (subsection IV.C.), our coil system has a calibrated workspace of 2 mm-radius sphere, and as a result, we tested the capsule prototype motion over small distances of $\pm$1 mm for planar displacements (x, y) and $\pm$10 deg for rotational maneuvers (yaw, $pitch$). Each one of the three cylindrical magnets can also move 2 mm inside their chambers before reaching their physical endpoints.

As presented in Fig. 5, the yaw angle actuation was tested first, with the desired trajectory changing from 0 to 10 deg (linear ramp profile), 10 to -10 deg and -10 to 0 deg. The yaw angle followed the desired trajectory and the other six DOFs remained close to zero. Next, x and then y positioning was tested, with the desired trajectory changing from 0 to 1 mm, 1 to -1 mm and -1 to 0 mm. The data shows that

TABLE III
CROSS-TALK REPORT; CALCULATED FOR EACH OF THE SEVEN DOFS AS: MAXIMUM DEVIATION DURING INACTIVE PERIODS DIVIDED BY CORRESPONDING MAXIMUM VALUE DURING THEIR DESIGNATED ACTIVE ACTUATION PERIODS. (FOR THE FIRST SIX ACTUATION PERIODS (COLUMNS 2-7) THE *roll* AND CONSEQUENTLY THE *pitch* AXIS WERE RESTRICTED.)

Exp.	*yaw*%	*x*%	*y*%	*d3*%	*d2*%	*d1*%	*pitch*%	All
1 (Mean)	8.08	7.23	4.74	8.22	8.15	7.62	4.57	7.04
1 (Max)	16.9	11.6	10.1	17.2	17.3	18.2	17.6	18.2
2 (Mean)	7.98	7.43	4.82	7.98	8.53	7.55	4.65	6.99
2 (Max)	17.5	10.1	10.1	17.3	17.2	18.1	17.8	18.1
3 (Mean)	8.04	7.62	4.88	8.03	8.63	7.58	4.66	7.06
3 (Max)	17.6	11.2	10.2	17.2	17.6	18.3	17.8	18.3

the robot followed desired x and y trajectories, while other DOFs remained close to zero. The releasing mechanism was tested next (the previously mentioned agitating field $\vec{B}_{ag}$ was enabled during this period, making the movement of cylindrical magnets inside drug reservoirs smoother). The desired position of magnets were defined at the end of tube chambers; i.e. traveling 2 mm inside the chambers. To move the magnets back and forth, injection forces were set (using trial and error method in a prior calibration experiment), as $f^*_{p_1} = f^*_{p_2} = f^*_{p_3} = \pm 150$ μN. The magnets' traveled distances, denoted as *d1*, *d2*, and *d3*, were measured during their activation periods, and as illustrated in Fig. 5, when each of the magnets was actuated, the rest of six DOFs remained close to zero. At the end, the $pitch$ angle actuation was tested, where the experiment was paused and more fluid (corn syrup mixed with water 10:3) was added into the acrylic container. This addition was not done in previous actuation periods, due to the insufficient feedback rate on the $roll$ axis of the robot. Since the $roll$ axis is not controllable, undesired orientation disturbances are seen. As a result and to restrict the $roll$ axis undesired effects, the container was filled with less fluid (just enough to enable the robot slide underneath and not float; i.e. restricted $roll$ and consequently $pitch$ axis) for the previous six actuation periods, and more fluid was added only for the $pitch$ actuation period, so that the robot can float and exhibit $pitch$ axis rotation. For this $pitch$ angle actuation, the reference trajectory was defined same as yaw angle (linear ramp profile $\pm$10 deg), and as shown in Fig. 5 (brown solid line), the $pitch$ angle followed the reference trajectory, while other six DOFs remained close to zero.

To study the microrobot's performance in terms of independent controllability of its DOFs, we measured the cross-talk for each of the seven DOFs. The cross-talk is defined here as the maximum deviation for each of the DOFs during its "inactive" period, divided by its maximum value during its "active" actuation period. For each DOF in this experiment, there are six inactive periods and one active period, resulting in six cross-talk measurements for each of the seven DOFs. The mean and maximum of these six cross-talk errors are presented in Table III, for three repeated experiment of the same type (representative trial #1 is shown in Fig. 5). The maximum mean cross-talk belongs to *d2* in Exp.#3 which

is 8.63%, and maximum cross-talk (not averaged) appears in Exp.#3, belonging to *d1* which is 18.3%.

V. CONCLUSIONS

We demonstrated a general framework to design dexterous magnetic microrobots for applications where external magnetic field sources are located relatively far from the targeted workspace; such as medical applications where magnetic field generation sources are located around patient's body, and a multi-DOF microrobot is required to deliver certain dosages of different drugs, perform biopsy, cut tissues, etc.

The presented framework utilizes both magnetic torque and magnetic forces, providing the maximum possible dexterity. However, it has two major limitations in comparison with approaches using only magnetic torques; first, most resulting designs would require real-time orientation feedback (we expect a rate of 60 Hz in low viscosity environments such as water) of the solid body of the microdevice to accurately control magnetic forces. This is a relatively high frame rate, therefore, one particular direction for future studies is to design axi-symmetric devices where orientation feedback error can be tolerated. Second, the magnetic force decays ($\propto l_w^{-4}$) faster than magnetic torque ($\propto l_w^{-3}$) as distance to targeted workspace (l_w) increases [26]. This relatively poorer scaling of magnetic forces with distance may make it difficult to design strong-enough mechanisms utilizing the five gradient terms of the field for some applications. Thus, it is recommended in general to actuate the mechanisms which require the largest force using the magnetic field (torque) components of the field while the gradient be used for weaker aspects of the application.

The modeling in our work does not include fluid interactions and dynamics and here we conduct our experiments at low velocity to avoid non-linear affects. Implementation works to follow this manuscript will explore the use of the presented design framework in the design of multi-DOF functional micro- and milli-robots operating with complex mechanisms where fluid dynamics will play a role. Another direction for future work will be investigating the sensitivity of the proposed method to microrobot orientation feedback error, and potentially extending the design optimization to be less vulnerable to this feedback error. Another area for future work will be utilizing the presented framework for soft-body (flexible) microrobots, where more DOFs can result in features such as more advanced locomotion patterns.

TABLE IV
VARIABLES GLOSSARY.

Var.	Description	Var.	Description
$\vec{B}$	magnetic field vector	$\vec{g}$	five magnetic gradient terms
$\vec{m}$	magnetization vector	$\mathbf{S}(\vec{m})$	skew-symmetric matrix
$\vec{\tau}$	torque vector	$\vec{f}$	force vector
$\mathbf{K}(\vec{m})$	wrench function matrix	$\vec{U}$	magnetic actuation input vector
n_{strip}	number of flexible strips	d_s	flexible strip deflection
n_{rod}	number of flexible rods	$d_{r1,2}$	flexible rod deflection
n_{slider}	number of sliders	f_p	slider (prismatic) force
$\vec{f}_s$	solid body total force vector	$\vec{\tau}_s$	solid body total torque vector
$\vec{f}_{\text{sel}}$	solid body selected force vector	$\vec{\tau}_{\text{sel}}$	solid body selected torque vector
$\mathbf{E1}$	force selecting matrix	$\mathbf{E2}$	torque selecting matrix
n_{sp}	number of selected forces	n_{so}	number of selected torques
$\vec{Y}$	microdevice output vector	n_D	total number of controlled DOFs
α	force to deflection converting scalar	β	torque to deflection converting scalar
$\hat{a}_i$	force projection unit vector for flexible strips	$\hat{b}_i$	torque projection unit vector for flexible strips
$\hat{a}_j$	force and torque projection unit vector for flexible rods	$\hat{b}_j$	force and torque projection unit vector for flexible rods
$\hat{a}_k$	force projection unit vector for sliders	$\vec{p}$	position vector
$\mathbf{H}$	system matrix	σ_i	singular values of the system matrix
r	system matrix rank	$\mathbf{C}_{i,j,k}$	transmission matrices
λ, γ	weight adjusting scalars	ρ	microrobot size limit
f_{int}	interaction forces scalar function	τ_{int}	interaction torques scalar function
$\mathbf{L}$	coil matrix	*d1,2,3*	magnets' traveled distances (for the drug delivery robot)

REFERENCES

[1] F. Munoz, G. Alici, and W. Li, "A review of drug delivery systems for capsule endoscopy," *Advanced drug delivery reviews*, vol. 71, pp. 77–85, 2014.

[2] C. Forbrigger, A. Lim, O. Onaizah, S. Salmanipour, T. Looi, J. Drake, and E. D. Diller, "Cable-less, magnetically-driven forceps for minimally invasive surgery," *IEEE Robotics and Automation Letters*, vol. 4, no. 2, pp. 1202–1207, 2019.

[3] O. Youssefi and E. D. Diller, "Contactless robotic micromanipulation in air using a magneto-acoustic system," *IEEE Robotics and Automation Letters*, vol. 4, no. 2, pp. 1580–1586, 2019.

[4] E. Diller, M. Sitti *et al.*, "Micro-scale mobile robotics," *Foundations and Trends in Robotics*, vol. 2, no. 3, pp. 143–259, 2013.

[5] V. M. Fomin, M. Hippler, V. Magdanz, L. Soler, S. Sanchez, and O. G. Schmidt, "Propulsion mechanism of catalytic microjet engines," *IEEE Transactions on Robotics*, vol. 30, no. 1, pp. 40–48, 2014.

[6] X. Li, C. Liu, S. Chen, Y. Wang, S. H. Cheng, and D. Sun, "In vivo manipulation of single biological cells with an optical tweezers-based manipulator and a disturbance compensation controller," *IEEE Transactions on Robotics*, vol. 33, no. 5, pp. 1200–1212, 2017.

[7] E. Y. Erdem, Y.-M. Chen, M. Mohebbi, J. W. Suh, G. T. Kovacs, R. B. Darling, and K. F. Bohringer, "Thermally actuated omnidirectional walking microrobot," *Journal of Microelectromechanical Systems*, vol. 19, no. 3, pp. 433–442, 2010.

[8] M. P. Kummer, J. J. Abbott, B. E. Kratochvil, R. Borer, A. Sengul, and B. J. Nelson, "Octomag: An electromagnetic system for 5-dof wireless micromanipulation," *IEEE Trans. on Robotics*, vol. 26, no. 6, pp. 1006–1017, 2010.

[9] J. J. Abbott, E. Diller, and A. J. Petruska, "Magnetic methods in robotics," *Annual Review of Control, Robotics, and Autonomous Systems*, vol. 3, 2020.

[10] P. Ryan and E. Diller, "Magnetic actuation for full dexterity microrobotic control using rotating permanent magnets," *IEEE Transactions on Robotics*, vol. 33, no. 6, pp. 1398–1409, 2017.

[11] E. Diller, J. Giltinan, G. Z. Lum, Z. Ye, and M. Sitti, "Six-degree-of-freedom magnetic actuation for wireless microrobotics," *The International Journal of Robotics Research*, vol. 35, no. 1-3, pp. 114–128, 2016.

[12] D. Wong, E. B. Steager, and V. Kumar, "Independent control of identical magnetic robots in a plane," *IEEE Robotics and Automation Letters*, vol. 1, no. 1, pp. 554–561, 2016.

[13] F. Ongaro, S. Pane, S. Scheggi, and S. Misra, "Design of an electromagnetic setup for independent three-dimensional control of pairs of

identical and nonidentical microrobots," *IEEE transactions on robotics*, vol. 35, no. 1, pp. 174–183, 2018.
[14] D. Son, M. D. Dogan, and M. Sitti, "Magnetically actuated soft capsule endoscope for fine-needle aspiration biopsy," in *2017 IEEE International Conference on Robotics and Automation (ICRA)*. IEEE, 2017, pp. 1132–1139.
[15] S. Yim, E. Gultepe, D. H. Gracias, and M. Sitti, "Biopsy using a magnetic capsule endoscope carrying, releasing, and retrieving untethered microgrippers," *IEEE Transactions on Biomedical Engineering*, vol. 61, no. 2, pp. 513–521, 2014.
[16] A. Becker, O. Felfoul, and P. E. Dupont, "Simultaneously powering and controlling many actuators with a clinical mri scanner," in *IEEE/RSJ Int. Conf. on Intell. Robots and Syst.*, 2014, pp. 2017–2023.
[17] D. R. Frutiger, K. Vollmers, B. E. Kratochvil, and B. J. Nelson, "Small, fast, and under control: wireless resonant magnetic micro-agents," *The International Journal of Robotics Research*, vol. 29, no. 5, pp. 613–636, 2010.
[18] M. Salehizadeh and E. Diller, "Two-agent formation control of magnetic microrobots in two dimensions," *Journal of Micro-Bio Robotics*, vol. 12, no. 1-4, pp. 9–19, 2017.
[19] S. Chowdhury, B. V. Johnson, W. Jing, and D. J. Cappelleri, "Designing local magnetic fields and path planning for independent actuation of multiple mobile microrobots," *Journal of Micro-Bio Robotics*, vol. 12, no. 1-4, pp. 21–31, 2017.
[20] J. Rahmer, C. Stehning, and B. Gleich, "Spatially selective remote magnetic actuation of identical helical micromachines," *Science Robotics*, vol. 2, no. 3, 2017.
[21] E. Diller and M. Sitti, "Three-dimensional programmable assembly by untethered magnetic robotic micro-grippers," *Advanced Functional Materials*, vol. 24, no. 28, pp. 4397–4404, 2014.
[22] F. Carpi and C. Pappone, "Stereotaxis niobe® magnetic navigation system for endocardial catheter ablation and gastrointestinal capsule endoscopy," *Expert review of medical devices*, vol. 6, no. 5, pp. 487–498, 2009.
[23] S. Jeon, A. K. Hoshiar, K. Kim, S. Lee, E. Kim, S. Lee, J.-y. Kim, B. J. Nelson, H.-J. Cha, B.-J. Yi *et al.*, "A magnetically controlled soft microrobot steering a guidewire in a three-dimensional phantom vascular network," *Soft robotics*, vol. 6, no. 1, pp. 54–68, 2019.
[24] A. W. Mahoney and J. J. Abbott, "Five-degree-of-freedom manipulation of an untethered magnetic device in fluid using a single permanent magnet with application in stomach capsule endoscopy," *The International Journal of Robotics Research*, vol. 35, no. 1-3, pp. 129–147, 2016.
[25] J. Giltinan and M. Sitti, "Simultaneous six-degree-of-freedom control of a single-body magnetic microrobot," *IEEE Robotics and Automation Letters*, vol. 4, no. 2, pp. 508–514, 2019.
[26] S. Salmanipour and E. Diller, "Eight-degrees-of-freedom remote actuation of small magnetic mechanisms," in *IEEE International Conference on Robotics and Automation (ICRA)*, 2018, pp. 3608–3613.
[27] A. N. Zelikin, C. Ehrhardt, and A. M. Healy, "Materials and methods for delivery of biological drugs," *Nature chemistry*, vol. 8, no. 11, pp. 997–1007, 2016.
[28] H. J. Lee, N. Choi, E.-S. Yoon, and I.-J. Cho, "Mems devices for drug delivery," *Advanced drug delivery reviews*, vol. 128, pp. 132–147, 2018.
[29] H. Zhang, J. K. Jackson, and M. Chiao, "Microfabricated drug delivery devices: Design, fabrication, and applications," *Advanced Functional Materials*, vol. 27, no. 45, p. 1703606, 2017.
[30] Y. Zhang, Y. Chen, Y. Qi, D. Huang, M. Yang, X. Yu, Y. Hu, and Z. Li, "An ocular iontophoretic device using pedot electrode for local drug delivery," *Sensors and Actuators B: Chemical*, vol. 237, pp. 1007–1014, 2016.
[31] J. Xi, X. A. Si, and R. Gaide, "Electrophoretic particle guidance significantly enhances olfactory drug delivery: a feasibility study," *PLoS One*, vol. 9, no. 1, p. e86593, 2014.
[32] H. Shin, H. J. Lee, U. Chae, H. Kim, J. Kim, N. Choi, J. Woo, Y. Cho, C. J. Lee, E.-S. Yoon *et al.*, "Neural probes with multi-drug delivery capability," *Lab on a Chip*, vol. 15, no. 18, pp. 3730–3737, 2015.
[33] S. H. Lee, Y. B. Lee, B. H. Kim, C. Lee, Y. M. Cho, S.-N. Kim, C. G. Park, Y.-C. Cho, and Y. B. Choy, "Implantable batteryless device for on-demand and pulsatile insulin administration," *Nature communications*, vol. 8, no. 1, pp. 1–10, 2017.
[34] S. P. Woods and T. G. Constandinou, "Wireless capsule endoscope for targeted drug delivery: mechanics and design considerations," *IEEE Transactions on Biomedical Engineering*, vol. 60, no. 4, pp. 945–953, 2013.
[35] C. T. Dietzel, H. Richert, S. Abert, U. Merkel, M. Hippius, and A. Stallmach, "Magnetic active agent release system (maars): evaluation of a new way for a reproducible, externally controlled drug release into the small intestine," *Journal of controlled release*, vol. 161, no. 3, pp. 722–727, 2012.
[36] S. Yim, K. Goyal, and M. Sitti, "Magnetically actuated soft capsule with the multimodal drug release function," *IEEE/ASME Trans. Mechatronics*, vol. 18, no. 4, pp. 1413–1418, 2013.
[37] S. Yim and M. Sitti, "Design and rolling locomotion of a magnetically actuated soft capsule endoscope," *IEEE Transactions on Robotics*, vol. 28, no. 1, pp. 183–194, 2012.
[38] A. J. Petruska and B. J. Nelson, "Minimum bounds on the number of electromagnets required for remote magnetic manipulation," *IEEE Transactions on Robotics*, vol. 31, no. 3, pp. 714–722, 2015.

Sajad Salmanipour received the B.S. degree in electrical engineering from Amirkabir University of Technology, Tehran, Iran, in 2011, the M.S. degree in electrical engineering from McMaster University, ON, Canada, in 2013 and the Ph.D. degree in mechanical engineering from University of Toronto, ON, Canada, in 2019. He received the Doctoral Completion Award from the Mechanical & Industrial Engineering Department in 2019. He has also received the Queen Elizabeth Dupont Canada Scholarship In Science And Technology, Mr. John H. Weber And Dr. Eleanor Connie Mariano Graduate Scholarship In Biomedical Engineering, Barbara And Frank Milligan Graduate Fellowship, and Ontario Graduate Scholarship. He is currently with ISEE Inc. as robotics engineer, where he develops control software for autonomous vehicles.

Omid Youssefi received his B.A.Sc. and M.A.Sc. in mechanical engineering from the University of Toronto in 2016 and 2019, respectively. As a result of his graduate work, he invented a new class of microrobotic manipulation method for performing contactless and semi-autonomous microassembly in air. In addition to journal, conference, and book chapter publications, his work was also selected as the best paper finalist award in the IEEE International Conference on Robotics and Automation in May 2019. After completing his masters degree, he joined Scentroid where he currently leads the research and development department.

Eric Diller received the B.S. and M.S. degree in mechanical engineering from Case Western Reserve University in 2010 and the Ph.D. degree in mechanical engineering from Carnegie Mellon University in 2013. He is currently Associate Professor and Dean's Catalyst Professor in the Department of Mechanical and Industrial Engineering at the University of Toronto, where he is director of the Microrobotics Laboratory. His research interests include micro-scale robotics, and features fabrication and control relating to remote actuation of micro-scale devices using magnetic fields, micro-scale robotic manipulation, smart materials. He is an Associate Editor of the Journal of Micro-Bio Robotics and received the award for Best Associate Editor at the 2015 IEEE International Conference on Automation and Robotics, as well as the IEEE Robotics & Automation Society 2020 Early Career Award. He has also received the 2018 Ontario Early Researcher Award, the University of Toronto 2017 Connaught New Researcher Award, and the Canadian Society of Mechanical Engineering's 2018 I.W. Smith Award for research contributions in medical microrobotics.